Proceedings of the ASME 2019
13th International Conference on Energy Sustainability
ES2019
July 15-17, 2019, Bellevue, WA, USA

SAND2019-10125C

ES2019-3910

EFFECT OF QUARTZ APERTURE COVERS ON THE FLUID DYNAMICS AND THERMAL EFFICIENCY OF FALLING PARTICLE RECIEVERS

Lindsey Yue[1], Brantley Mills, Clifford K. Ho
Sandia National Laboratories
Albuquerque, NM, USA

ABSTRACT

Falling particle receivers are an emerging technology for use in concentrating solar power systems. In this work, quartz tubes cut in half to form tube shells (referred to as quartz half-shells) are investigated for use as a full or partial aperture cover to reduce radiative and advective losses from the receiver. A receiver subdomain and surrounding air volume are modeled using ANSYS® Fluent®. The model is used to simulate fluid dynamics and heat transfer for the following cases: (1) open aperture, (2) aperture fully covered by quartz half-shells, and (3) aperture partially covered by quartz half-shells. We compare the percentage of total incident solar power lost due to conduction through the receiver walls, advective losses through the aperture, and radiation exiting out of the aperture. Contrary to expected outcomes, simulation results using the simplified receiver subdomain show that quartz aperture covers can increase radiative losses and, in the partially covered case, also increase advective losses. These increased heat losses are driven by elevated quartz half-shell temperatures and have the potential to be mitigated by active cooling and/or material selection.

Keywords: concentrated solar power, falling particle receiver, thermal efficiency, aperture cover, numerical modeling.

NOMENCLATURE

c_p	specific heat capacity (J kg^{-1} K^{-1})
k	thermal conductivity (W m^{-1} K^{-1})
$\dot{m}$	mass flow rate (kg s^{-1})
n	real part of the refractive index
q	heat rate (W)
T	temperature (K or °C)
α	absorptivity
ε	emissivity
η	thermal efficiency
λ	subscript indicating spectral quantities
ρ	density (kg m^{-3})
τ	transmissivity

INTRODUCTION

Falling particle receivers (FPR) are an emerging technology for use in concentrating solar power (CSP) systems [1]. FPRs have the potential to operate at higher temperatures than current direct-steam or molten-salt receivers, thus increasing the maximum potential operating temperature of the CSP power cycle and the solar-to-electric efficiency [2]. However, higher-temperature receivers may also experience greater heat losses, both radiative and advective, through the aperture. In this work, fused quartz tubes cut in half to form tube shells (referred to as quartz half-shells) are investigated for use as a full or partial aperture cover to reduce radiative and advective losses from the receiver.

Fused quartz is mostly transparent to solar radiation and mostly opaque to the expected thermal radiation emitted by the receiver walls and falling particles [3]. Thus, it is a suitable material for obstructing radiation emitted by the receiver interior while theoretically minimally reducing concentrated solar radiation entering the receiver. Aperture covers consisting of quartz half-shells are considered rather than covers consisting of flat quartz panes for the increased strength and potential for concentrating/light trapping of the half-shell shape.

The simulated system is a simplified subdomain of a complete FPR and the surrounding air space. The system is modeled after an existing, north-facing 1 MW_{th} FPR at the

[1] Contact author: lyue@sandia.gov

National Solar Thermal Test Facility (NSTTF) at Sandia National Laboratories [4]. The NSTTF FPR cavity is 1.78 m tall, 1.57 m wide, and 1.7 m deep with a north facing, 1 m square aperture opening. Radiation enters the receiver from a field of 200 heliostats, capable of supplying up to 6 MW_{th}. Particles enter the receiver from above the receiver cavity and fall freely from a slot, passing through the receiver cavity and radiation beam from the heliostat field. The particles are irradiated as they fall through the receiver cavity, resulting in particle heating.

The idealized subdomain considered in this analysis is a vertical slice, 0.11 m wide in the east–west direction, taken at the center of the receiver. The central east–west location experiences the most irradiation compared to other lateral locations due to the paraboloidal shape of the intensity of radiation coming from the heliostat field. The central location is also the most thermally insulated location on the east and west sides. This location at the center of the receiver is therefore expected to have a higher efficiency than those at locations off center as well as that of the entire receiver.

The receiver subdomain and surrounding air volume are modeled using ANSYS® Fluent®. The model is used to simulate fluid dynamics and heat transfer for the following cases: (1) open aperture, (2) aperture fully covered by quartz half-shells, and (3) aperture partially covered by quartz half-shells. We compare the percentage of total solar power entering the aperture that is lost due to conduction through the receiver walls, advective losses through the aperture, and radiation exiting out of the aperture. The aim of this work is to quantify the relative impact of quartz half-shell aperture covers on the thermal efficiency and heat loss mechanisms of the FPR, with the goal of improving receiver thermal efficiency.

For the assumed subdomain system, we found that elevated quartz half-shell temperatures in the fully and partially covered cases drive increased heat losses when compared to the open aperture case. Radiative losses increase in both the fully and partially covered cases compared to the open aperture case. Advective losses also increase in the partially covered case compared to the open aperture case. Because losses are increased in the fully and partially covered cases, the thermal efficiency of those cases is reduced. Reducing the temperature of the quartz half-shells has the potential to mitigate these increased heat losses. In addition, increased quartz half-shell temperatures may be a result of the simplified geometry, which forces a significant amount of reflected and emitted radiation from the interior walls to leave through the aperture and heat the quartz half-shells. Additional three-dimensional modeling of the entire receiver cavity should be performed to evaluate the 'cavity effect,' which may reduce radiative losses and heating of the quartz half-shells.

1 Computational Model

The system geometry and materials are first presented in this section. Next, the modeling methods used to capture the physical phenomena relevant to the application are described. For additional information about the governing equations and closure models discussed here, the reader is referred to the modeling tool, ANSYS® Fluent®, documentation [5]. Similar modeling approaches have been used to describe the fluid dynamics, particle flow, and heat transfer in FPRs [6][7][8], including models yielding results that have been favorably compared to experiments [9][10][11]. This history supports the validity of the modeling approach used in this work.

1.1 System geometry and materials

The simulated system is a 0.11 m wide subdomain of the NFTTF FPR and a volume of surrounding air. The subdomain receiver is shown in Figure 1 from the west. The subdomain is sufficiently narrow in the east–west direction compared to the width of the FPR that we assume symmetric boundary conditions on the east and west faces of the system to simplify the model.

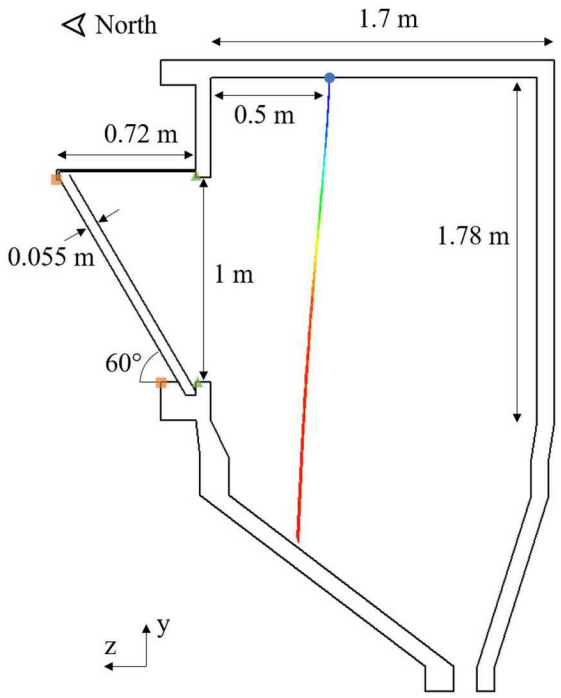

FIGURE 1: SUBDOMAIN CROSS SECTION WITH QUARTZ HALF-SHELL APERTURE COVER AND HYPOTHETICAL PARTICLE TRACKS COLORED BY PARTICLE TEMPERATURE; PARTICLE INJECTION POINT IS MARKED BY A BLUE CIRCLE; POINTS DEFINING THE 'HOOD APERTURE' ARE MARKED BY ORANGE SQUARE POINTS; AND POINTS DEFINING THE 'RECEIVER APERTURE' ARE MARKED BY GREEN TRIANGLE POINTS

The aperture cover is made up of thin fused quartz half-shells. The half-shell wall thickness is 0.0025 m, and the shell diameter is 0.11 m. Properties of fused quartz used in this analysis are given in Table 1. The half-shells span from the northern edge of the receiver hood to the bottom of the aperture opening, and the shape of the ends of the half-shells conforms to the bounding receiver walls, shown in the receiver schematic in Figure 1. The length of the half-shells creates a 60° angle with the horizon, and the concave side of the half-shells faces north.

In practice, half-shell ends will likely be flat and oriented perpendicular to the length, but the geometry was altered to simplify meshing and analysis. This simplification likely results in overestimated reductions in advective losses.

TABLE 1: PROPERTIES OF FUSED QUARTZ

Property	Value	Units	Source
ρ	2200	kg m^{-3}	[12]
c_p	Piecewise-Linear Profile: 772@100°C 964@500°C 1052@900°C	J kg^{-1} K^{-1}	[12]
k	Piecewise-Linear Profile: 1.38@20°C 1.46@100°C 1.55@200°C 1.67@300°C 1.84@400°C 2.68@950°C	W m^{-1} K^{-1}	[12]
τ_λ	0.9 (λ=0–2.5 μm) 0.5 (λ=2.5–4.5 μm) 0.1 (λ=4.5–100 μm)		[3]
n_λ	1.50 (λ=0–2.5 μm) 1.42 (λ=2.5–4.5 μm) 1.41 (λ=4.5–100 μm)		[12]

Two planes were defined and used to evaluate the receiver thermal efficiency. The first plane is referred to as the 'hood aperture.' It sits just north of the quartz half-shells and is defined by the northern top-most point of the lower receiver volume and the northern bottom most-point of the end of the aperture hood, marked with orange square points in Figure 1. The second plane is referred to as the 'receiver aperture' and is defined by the northern most edges of the receiver cavity opening, marked with green triangle points in Figure 1.

TABLE 2: PROPERTIES OF FIBERFRAX® DURABOARD® HD

Property	Value	Units	Source
ρ	420	kg m^{-3}	[13]
c_p	1000	J kg^{-1} K^{-1}	[13]
k	Piecewise-Linear Profile: 0.075@204°C 0.1@427°C 0.14@649°C 0.19@871°C 0.22@982°C	W m^{-1} K^{-1}	[13]
$\alpha_\lambda/\varepsilon_\lambda$	0.1 (λ=0–2.5 μm) 0.4 (λ=2.5–4.5 μm) 0.8 (λ=4.5–100 μm)		[13]–[14]

The size of the volume of air surrounding the receiver is selected to be sufficiently large that boundary effects do not influence fluid dynamics near the receiver. The considered volume of air extends 2 m north of the end of the aperture hood, 1 m above the top of the receiver, and 0.98 m south of the south receiver wall. The air volume does not extend below the bottom of the particle collection hopper below the receiver.

The receiver walls are treated as solid continuous volumes with the properties of Fiberfrax® Duraboard® HD, a high temperature alumina–silica fiber board. Properties of Fiberfrax® Duraboard® HD are given in Table 2.

1.2 Fluid dynamics model

Turbulent flow of air is modeled using the realizable k–ε turbulence model which has previously been used to model fluid dynamics of the entire NFTTF FPR with good agreement between experimental and numerical results [15]. Scalable wall functions are applied to reduce the effects of mesh size on fluid dynamics near the wall.

1.3 Particle model

The falling particles are modeled as a discrete phase, entering the receiver from 30 injection sites spanning the east–west width of the subdomain system, located 0.5 m south of the aperture. The location of the injection sites is marked with a blue circle point on the receiver schematic in Figure 1. Particles enter the system at a temperature of 500 K or 227°C with a downward velocity of 3 m s^{-1} at a total flow rate of 1 kg s^{-1} and exit at first contact with a receiver wall. Effects due to particle bouncing in the collection hopper are therefore neglected in this analysis. Particle to particle interactions are also not included in the model, a valid approach for a discrete phase with a volume fraction less than 10% [15]. The particles are given a downward velocity to approximate particle acceleration between the discharge hopper (omitted from this analysis) and the receiver cavity. The total flow rate selected is approximately equivalent to a total flow rate of 10 kg s^{-1} m^{-1} for the entire receiver. This flow rate falls near the large end but still in the range of flow rates considered in experimental campaigns with the FPR [11]. Particles are given the properties of CARBO Accucast, a high-strength commercial ceramic particle previously used in FPR tests at the NSTTF. Particle properties are given in Table 3.

TABLE 3: PROPERTIES OF CARBO ACCUCAST [9]

Property	Value	Units
ρ	3550	kg m^{-3}
c_p	Piecewise-Linear Profile: 947@200°C 1073@400°C 1136@550°C	J kg^{-1} K^{-1}
ε	0.8	
scattering factor	0.3	
mean diameter	300	μm

1.4 Heat transfer model

Radiative heat transfer in the system is modeled using a non-grey discrete ordinate model. The receiver wall volumes are modeled as non-participating; air is modeled as non-absorbing and non-scattering with a refractive index of unity; and the quartz half-shells are modeled as non-scattering, semi-transparent

media. Incidence angle-dependent specular reflection is modeled at quartz–air interfaces using Snell's Law and the Fresnel equations [5].

Three spectral bands are considered in the radiation model: 0–2.5, 2.5–4.5, and 4.5–100 μm. The 2.5 μm cut off wavelength is selected to distinguish the solar spectrum: all solar radiation is defined in the first spectral band. This cut off wavelength also represents a transition in optical behavior of fused quartz. The 4.5 μm cutoff wavelength represents the transition in optical behavior of Fiberfrax® Duraboard® HD. The 100 μm cut off wavelength is selected to account for the majority of thermal emissions of the receiver interior and particles. Polar and azimuthal ordinate dimensions are both discretized into seven divisions and three pixels per octant.

Optical radiative performance of the entire FPR with quartz half-shell aperture covers has been modeled using ray tracing [16]. Ray tracing results will be used in future analyses to define heat source terms for the receiver walls and particle curtain in the receiver subdomain model presented here. This will be done to (1) more accurately represent radiation from the heliostat field and radiative transfer in the receiver cavity and (2) interrogate the validity of using the non-grey three-band discrete ordinate model for this system.

1.5 Boundary conditions

The downward facing receiver walls and hopper exit are assumed adiabatic. All east and west facing boundaries are treated as symmetric. A beam of radiation originating from a section of the north system boundary is used to model solar radiation from the heliostat field. This beam is implemented using a semi-transparent wall at the lower section of the north boundary, through which the beam is transmitted. The beam is nearly collimated with a flux of 1 MW m^{-2} applied over an area measuring 0.11 m in the east–west direction and 1.07 m vertically. This results in radiative energy entering the entire system at a rate of 117 kW. The beam is applied in an upward direction of (0, 0.5, –0.866) to simulate the NSTTF tower and heliostat field. Of the 117 kW of radiative energy entering the system at this angle, 111 kW or 95% enters the receiver via the aperture plane. All other north, south, top, and bottom boundaries are treated as pressure boundary conditions that radiate at ambient temperature. Ambient temperature is 300 K or 27°C in this analysis.

2 Cases and numerical solution

Three cases are considered in this work. The baseline case is a receiver with no aperture covers and will be referred to as the 'no coverage' case. To consider the maximum extent to which aperture covers could affect thermal losses and receiver efficiency, a receiver aperture completely covered by adjacent quartz half-shells is considered and will be referred to as the 'full coverage' case. In addition to the two extreme cases, a receiver aperture covered by 50% with equally spaced quartz half-shells is also considered and will be referred to as the 'half coverage' case.

A single mesh containing two bisected adjacent quartz half-shells is used for all three cases. The mesh has 406,721 tetrahedral elements, concentrated around the thin quartz half-shells and air volume underneath the receiver hood, to provide adequate resolution in those regions. One or both of the bisected quartz half-shells are treated as air for the half and no coverage cases, respectively.

To interrogate mesh invariance, the no coverage case is solved using several different meshes composed of hexahedral and tetrahedral elements ranging from 766–3,384,288 and 27,498–22,927,050 elements, respectively. The rate of energy transferred to the particles is shown in Figure 2 for the no coverage case solved using all considered meshes. The rate of energy transferred to the particles asymptotically approaches a constant value as the number of elements increases. Other quantities of interest also exhibit similar trends. The difference in rate of energy transferred to the particles between the mesh used in this study (406,721 elements) and the mesh containing the most elements (22,927,050) is 4%. This margin was deemed acceptable, particularly relative to the decrease in computational cost, however, results presented in this work should be considered comparatively and not quantitatively, given the discrepancy between results obtained using different meshes.

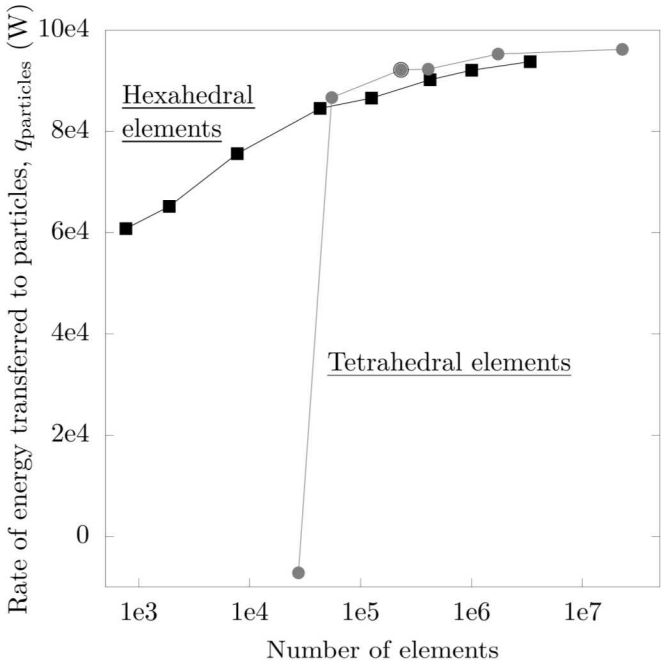

FIGURE 2: THE RATE OF ENERGY TRANSFERRED TO THE PARTICLES VERSUS THE NUMBER OF ELEMENTS IN THE MESH FOR ALL CONSIDERED HEXAHEDRAL (BLACK SQUARE POINTS) AND TETRAHEDRAL (GRAY CIRCLE POINTS) MESHS. THE BASELINE TETRAHEDRAL MESH IS INDICATED BY A LARGER BLACK CIRCLE AROUND THE GRAY CIRCLE POINT

The model is solved for steady state conditions until energy balances for the entire system to within 0.1%. Results, therefore, do not account for transient affects.

3 Results and Discussion

Results for three cases with different aperture coverage are presented and discussed in this section. Results include thermal losses and receiver thermal efficiency. Results for the investigation of model sensitivity to quartz volumetric transmissivity, radiation spillage, and receiver wall soiling are also presented and discussed.

3.1 Trends for all cases

Some trends can be observed in all three considered cases. Radiative power enters the hood aperture at a rate of 111 kW. Particle temperature increases as particles fall through the receiver cavity due to absorption of a portion of this incoming radiative power. Air in the receiver cavity is entrained in the particle curtain, leading to circulating flow in the receiver behind the curtain. The flow rotates counter clockwise when the receiver is viewed from the orientation of Figure 1. The interior regions of the receiver walls are elevated in temperature due to absorption of a portion of the incoming radiative power not absorbed by the particle curtain as well as due to heat exchange with the air inside the receiver. Air inside the receiver is elevated in temperature due to heat exchange with the particle curtain and receiver walls heated by absorbed radiation. A region of air behind the particle curtain is nearly uniform in temperature at a temperature near that of the particle curtain. This region is insulated from the ambient environment by the particle curtain and air circulation behind the particle curtain.

Air plumes rise from the north edge of the receiver hood in all considered cases. Air with elevated temperature under the hood drives the rising plume outside of the receiver. This air is replaced by lower temperature air crossing the hood aperture plane at the bottom of the hood aperture, resulting in advective losses.

While most of the radiation entering the system (117 kW) enters the receiver via the hood aperture (111 kW) and is then absorbed by the particle curtain, some radiation is incident on the front, north faces of the receiver. This radiation is referred to as spillage, and results in elevated temperatures of north facing external receiver walls near the hood and receiver apertures. The maximum temperature for all cases occurs at the same location: the wall at the top of the receiver aperture where the largest amount of radiation spillage is incident. This area is marked by the upper green triangle point in Figure 1.

Of the radiation incident on the interior receiver walls, a fraction is reflected, while that which is not reflected is absorbed. This absorption leads to interior wall regions of increased temperature relative to the temperature of regions of wall not in the path of the incoming radiative power, which are of a similar temperature to that of the air inside the receiver. There is a temperature gradient in the receiver walls from the interior (at temperatures around 330°C for all cases) to the exterior (27°C).

3.2 Thermal losses

Thermal losses occur by three mechanisms in the considered system: advection of enthalpy of air across the hood aperture, heat transfer through the receiver wall, and radiation leaving the aperture. The rate of heat flux integrated over the exterior receiver walls give the total power conducted through the receiver walls that is either convected away from the receiver wall exterior or net radiatively exchanged by the receiver wall exterior with the surroundings. These losses are collectively referred to as 'wall losses.' Radiative losses are quantified as the rate of radiation exiting the hood aperture.

Thermal losses as a percentage of the radiative power entering the hood aperture are shown in Figure 3. The smallest losses are due to heat transfer through the receiver walls. Wall losses increase with increasing aperture coverage because the temperature gradient across the hood increases slightly with increasing coverage due to the insulating effect of aperture coverage.

For all three cases, thermal losses due to radiation leaving the aperture are the largest by an order of magnitude over losses due to the other two mechanisms. This trend is contrary to previous numerical investigations of the full receiver without a hood which show advection as the mechanism resulting in the largest heat loss [11]. However, it should be noted, model results for this subdomain system show that inclusion of the hood increases the radiative power entering the receiver aperture as well as decreases advective losses which could explain the discrepancy between loss trends observed in this work compared to the previous investigations.

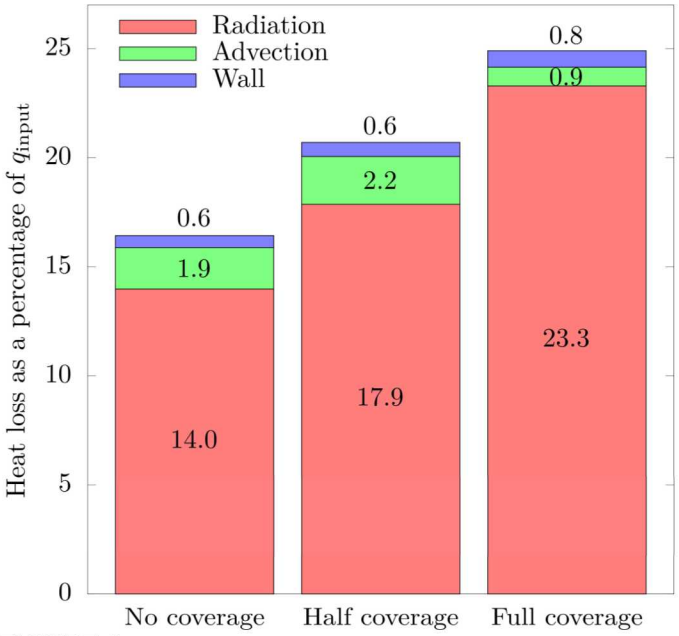

FIGURE 3: HEAT LOSS BY MECHANISM AS A PERCENTAGE OF INPUT RADIATIVE POWER ENTERING THE HOOD APERTURE FOR THE NO, HALF, AND FULL COVERAGE CASES; LOSSES ARE STACKED FROM THE BOTTOM IN THE FOLLOWING ORDER: RADIATION, ADVECTION, AND WALL

Radiative losses are also likely overestimated in this analysis because of the symmetric boundary condition assumption. In a three-dimensional cavity receiver, light

trapping will occur, and a portion of the radiation reflected diffusely off the back receiver walls will have the opportunity to be absorbed by the side walls. When assuming symmetric boundary conditions, all radiation incident on the symmetric boundaries (i.e. mostly from diffusely reflected radiation) is specularly reflected off the symmetry boundary [5]. If this reflected radiation is reflected laterally and not incident on the top or lower receiver walls, it will eventually exit the receiver aperture, contributing to overestimated radiative losses.

Radiative losses increase with increasing aperture coverage. This trend is contrary to our hypothesis that radiative losses would decrease in cases with aperture covers. The quartz half-shells likely do prevent some of the thermal emissive power from the receiver interior from being radiated to the ambient environment, but most of this radiation is prevented from reaching the ambient environment because it is absorbed in the quartz half-shells. Only a small fraction is reflected back into the receiver because reflectivity at the quartz–air interface for all wavelength bands is low (3–4% reflectivity for direct incidence).

While absorption of radiation due to thermal emissions in the 2.5–4.5 and 4.5–100 μm wavelength bands contributes to elevated quartz half-shell temperatures, quartz half-shell temperatures are primarily elevated due to absorption of radiation in the solar wavelength band. Although the transmissivity of fused quartz in the solar band is much higher than that in the longer wavelength bands (see Table 1), the amount of radiation in the quartz in the solar band is much larger than that in the longer wavelength bands. For the half and full coverage cases, 95% of radiation transmitted into the quartz volume from the north face of the quartz half-shells and 67% of radiation transmitted into the quartz volume from the south face of the quartz half-shells are in the solar band. This spectral delineation leads to a larger amount of absorbed radiation in the solar band than in the longer wavelength bands, even though the transmissivity in the solar band is higher than that in the longer wavelength bands. Thus, absorption of radiation in the solar band is the primary driver of elevated quartz half-shell temperatures.

Elevated quartz half-shell temperatures lead to increased thermal emissions. The view factor of the quartz to the ambient environment (nearly unity) is larger than the view factor of the receiver interior to the ambient environment (approximately 0.2), thus increases in quartz temperature and emissive power lead to greater radiative losses than the same increases in emissive power of the interior receiver walls. The quartz half-shells act as a 'short circuit' for radiative losses by moving the primary radiating body from a location with a small view factor to the ambient environment (the receiver interior) to a location with a large view factor to the ambient environment (the quartz half-shells).

The wavelength distribution of radiative losses supports the assertion that elevated quartz temperatures increase radiative losses due to increased quartz emissions. The wavelength of radiative losses shifts from the solar band to higher wavelengths with aperture coverage, indicating that the losses for the no coverage case are primarily due to incoming radiation being reflected while losses in cases with aperture cover contain larger contributions due to thermal emissions. This shift to higher wavelengths with increasing coverage can be seen in Figure 4, showing percentage of radiative loss in each wavelength band for the three cases.

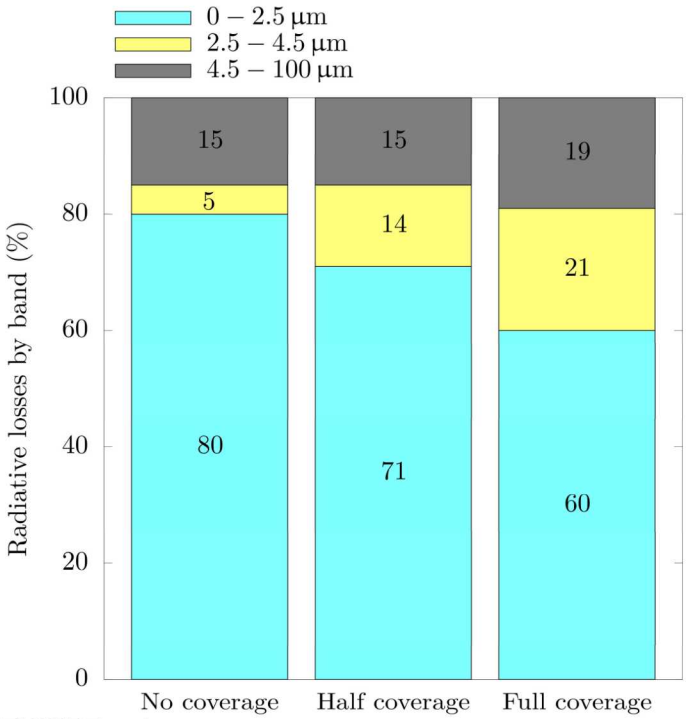

FIGURE 4: PERCENTAGE OF RADIATIVE LOSSES EVALUATED AT THE HOOD APERTURE BY WAVELENGTH BAND FOR THE NO, HALF, AND FULL COVERAGE CASES; LOSSES ARE STACKED FROM THE BOTTOM IN THE FOLLOWING ORDER: 0–2.5, 2.5–4.5, AND 4.5–100 μm

Elevated quartz half-shell temperature is the driving cause of elevated radiative losses in the cases with aperture covers compared to the no coverage case. In the half coverage case, elevated quartz half-shell temperature drives increased advective losses as well. The maximum and average temperature of the quartz half-shells are given in Table 4 for the half and full coverage cases. These elevated quartz half-shell temperatures raise system efficiency concerns because of increased losses, as well as raising material failure concerns. Maximum temperatures in the half and full coverage cases exceed the maximum working temperatures of some commercially available fused quartz products, which are around 1000°C [12]. Active cooling or alternative material selection may be necessary if such high temperatures are realized in actual tests.

TABLE 4: MAXIMUM AND AVERAGE QUARTZ TEMPERATURE FOR CASES WITH QUARTZ HALF-SHELLS

Case	Half coverage	Full coverage
T_{max}	1080°C	1170°C
T_{avg}	880°C	960°C

Of the considered cases, the half coverage case has the largest advective losses while the full coverage case has the smallest. The full coverage case was expected to have the smallest losses due to advection because the quartz half-shells block flow of air leaving and entering the receiver at high and low temperatures, respectively. The advective losses are not eliminated from this case, however, because the elevated temperature of the quartz half-shells just inside the hood aperture also causes local heating of adjacent air and natural convection. The upward flow caused by the natural convection results in advective losses across the hood aperture plane.

In the half coverage case, enthalpy exchange due to hot air from the receiver interior crossing the hood aperture (as observed in the no coverage case) and natural convection due to the hot quartz half-shell (as observed in the full coverage case) combine and both contribute to advective losses. The quartz half-shells in the half coverage case act essentially as fins, transferring energy to air flowing past when the quartz temperature is higher than the air temperature. The air temperature in this case is maximally around 330°C while the quartz half-shell temperatures exceed 800°C. The combination of both phenomena results in higher advective losses for the half coverage case compared to the no or full coverage cases.

3.3 Receiver thermal efficiency

Thermal efficiency for the receiver is defined as the ratio of the enthalpy transfer rate to the particles to the radiative power entering the hood aperture plane.

$$\eta = \frac{q_{\text{particles}}}{q_{\text{rad}}} \times 100\% \quad (1)$$

$$q_{\text{particles}} = \int_{T_{\text{in}}}^{T_{\text{out}}} \dot{m} c_{\text{p}} \mathrm{d}T \quad (2)$$

Thermal efficiencies for the no, half, and full coverage cases are 83, 78, and 75%, respectively, shown with green circle points in Figure 5. Radiative power entering the hood aperture is 111 kW for all three cases. The difference in thermal efficiency is therefore due to differences in the rate of enthalpy transfer to the particles and the thermal losses preventing incoming radiative energy from being transferred to the particles.

The objective of quartz half-shell aperture covers was to reduce losses and increase receiver efficiency. In this analysis, aperture covers only reduced one type of loss in one case when compared to the baseline no coverage case: advective losses decrease in the full coverage case. In the half and full coverage cases, the quartz half-shell aperture covers lead to increased radiative losses compared to the baseline case, and in the half coverage case, increased advective losses as well. These increased losses lead to reduced thermal efficiencies by up to 8.5% from the baseline no coverage case, contrary to the target objective. Increases to radiative losses in the cases with aperture covers are the primary contributor to reductions in thermal efficiency. Additional three-dimensional simulations will be performed to investigate the impact of the 'cavity effect' on radiative losses and quartz half-shell temperatures relative to the simplified subdomain model used in the current work. We expect radiative losses and quartz half-shell temperatures to be reduced for the three-dimensional geometry.

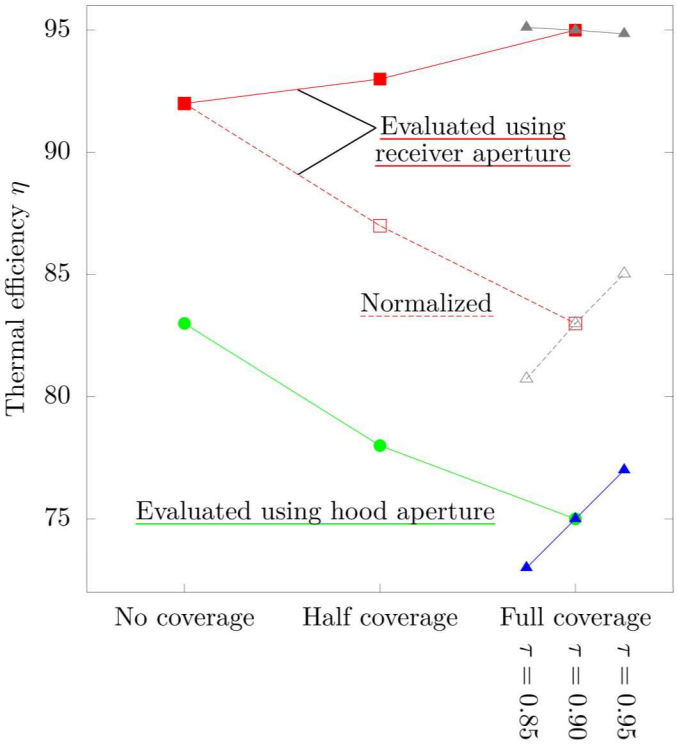

FIGURE 5: THERMAL EFFICIENCY EVALUATED USING THE RECEIVER APERTURE (FILLED RED SQUARE POINTS AND SOLID LINE), NORMALIZED TO NO COVERAGE CASE INPUT POWER (OPEN RED SQUARE POINTS AND DASHED LINE), HOOD APERTURE (GREEN CIRCLE POINTS AND LINE), AND FOR THE FULL COVERAGE CASE WITH VARYING VOLUMETRIC TRANSMISSIVITY IN THE SOLAR BAND (BLUE TRIANGLE POINTS AND LINE)

Receiver efficiency can also be evaluated using the receiver aperture plane. This plane has typically been used to evaluate cavity receiver efficiency in past studies. However, when applied to this analysis, the thermal efficiency evaluated using the receiver aperture does not account for losses due to quartz reflection or absorption, because the power entering the receiver is evaluated after radiation passes through the quartz. For completeness, thermal efficiency evaluated using the receiver aperture is reported: the thermal efficiencies for the no, half, and full coverage case are 92, 93, and 95%, respectively, shown with filled red square points in Figure 5. These receiver thermal efficiencies are nearly uniform, because the larger effects of the differences between the cases are not included in thermal efficiency evaluated using the receiver aperture plane. These differences include quartz reflection and absorption and natural convection around the hot quartz half-shells.

Radiative power entering the system, the hood aperture, and the receiver aperture are shown in Table 5, along with the rate of energy transferred to the particles. The difference between

power entering the system and the hood aperture is due to spillage. The difference between power entering the hood and receiver aperture in the no coverage case is also due to spillage. The difference between power entering the receiver aperture in the no coverage and half or full coverage cases is due to reflection and absorption by the quartz. Aperture covers are a component of the receiver, and it is the assertion of the authors that the effects of aperture covers should therefore be included in the determination of the receiver thermal efficiency.

TABLE 5: RADIATIVE POWER ENTERING THE SYSTEM FROM THE SOURCE, ENTERING THE RECEIVER FROM THE HOOD APERTURE, AND ENTERING THE RECEIVER FROM THE RECEIVER APERTURE, AND THE RATE OF ENERGY TRANSFERRED TO THE PARTICLES

Case	No coverage	Half coverage	Full coverage
q_{rad} source	117 kW	117 kW	117 kW
q_{rad} hood aperture	111 kW	111 kW	111 kW
q_{rad} receiver aperture	100 kW	93 kW	87 kW
$q_{particles}$	92 kW	87 kW	83 kW

Thermal efficiency evaluated using the receiver aperture can be normalized for the no, half, and full coverage cases by taking the radiative power entering the receiver aperture for the no coverage case (100 kW) as input radiative power in Equation (1). Evaluated in this manner, the thermal efficiencies for the no, half, and full coverage cases are 92, 87, and 83%, respectively, shown with open red square points in Figure 5. Thermal efficiency evaluated in this manner or using the hood aperture reflects that less energy is transferred to the particles in the cases with aperture covers.

Losses evaluated as a percentage of radiative power entering the receiver aperture are shown in Figure 6 for the considered cases. Wall losses are uniform for all considered cases. Radiative losses evaluated at the receiver aperture increase marginally with coverage due to slightly elevated temperatures in the receiver cavity. Percentage of radiative losses from the receiver aperture in each wavelength band are show in Figure 7. For the no coverage case, the percentage of radiative losses from the receiver aperture in each wavelength band remain the same when evaluated from the hood or receiver aperture. For the half and full coverage cases, the radiative losses are more dominated by solar reflections than those evaluated at the hood aperture, because the contribution of quartz thermal emissions to radiative losses is not included when evaluating losses at the receiver aperture. The differences in the wavelength distribution of radiative losses between cases are smaller when losses are evaluated at the receiver aperture than the hood aperture.

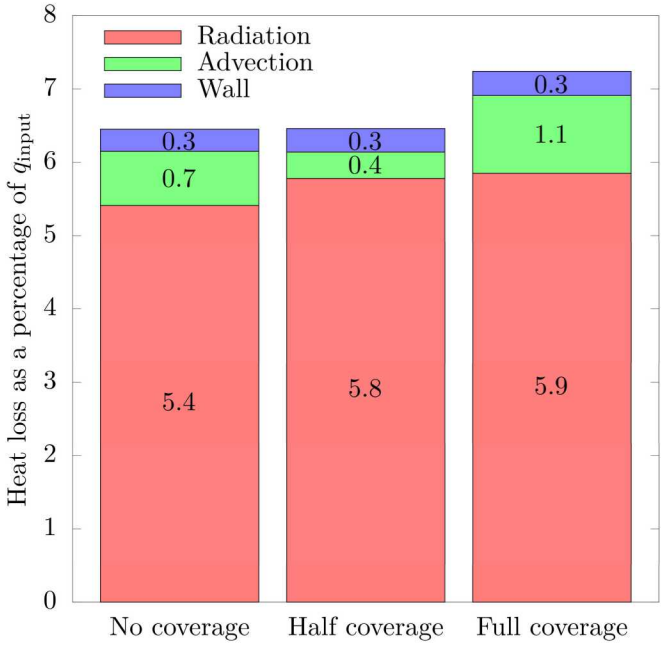

FIGURE 6: HEAT LOSS BY MECHANISM AS A PERCENTAGE OF INPUT RADIATIVE POWER ENTERING THE RECEIVER APERTURE FOR THE NO, HALF, AND FULL COVERAGE CASES; LOSSES ARE STACKED FROM THE BOTTOM IN THE FOLLOWING ORDER: RADIATION, ADVECTION, AND WALL

Advective losses evaluated at the receiver aperture show an opposite trend with coverage to those evaluated at the hood aperture: advective losses for the half coverage case are the lowest and for the full coverage case are the highest. Advective losses increase for the full coverage case because of circulation under the hood in the region enclosed by the aperture cover: an eddy forms bounded by the aperture cover, hood, and particle curtain, circulating clockwise when viewed from the orientation of Figure 1. This eddy is bisected by the receiver aperture plane, drawing lower temperature air into the receiver at the top of the receiver aperture plane and drawing higher temperature air out of the receiver at the bottom of the receiver aperture plane. For the half coverage case, the aperture cover reduces advective losses because the quartz half-shells act as hypothesized by obstructing and reducing the flow across the receiver aperture plane compared to the no coverage case, but not redirecting and circulating flow as in the full coverage case.

3.4 Model sensitivity to quartz volumetric transmissivity

Elevated quartz temperatures are driven by absorption of radiation in the solar band which then increases radiative losses. Transmissivity of fused quartz in the solar band can vary by manufacturer and has the potential to substantially change quartz half-shell temperatures and radiative losses, motivating the investigation of model sensitivity to quartz optical properties.

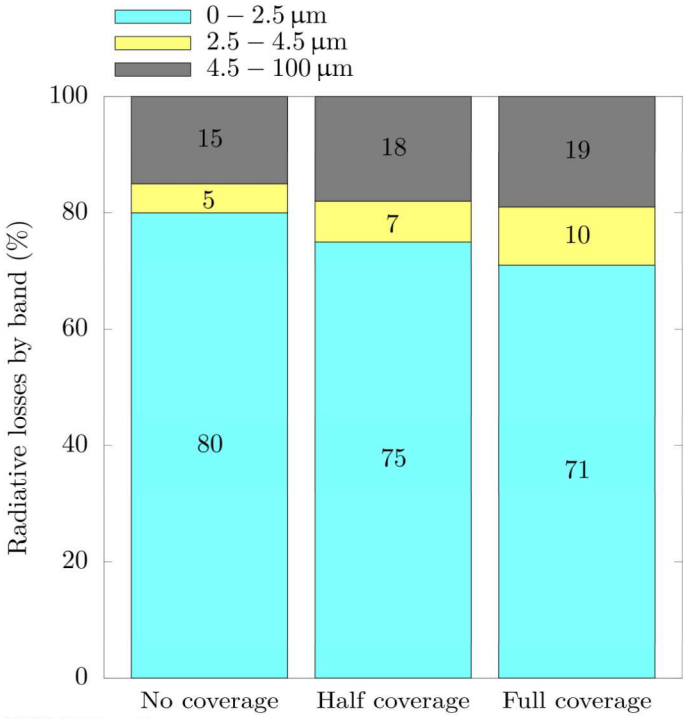

FIGURE 7: PERCENTAGE OF RADIATIVE LOSSES EVALUATED AT THE RECEIVER APERTURE BY WAVELENGTH BAND FOR THE NO, HALF, AND FULL COVERAGE CASES; LOSSES ARE STACKED FROM THE BOTTOM IN THE FOLLOWING ORDER: 0–2.5, 2.5–4.5, AND 4.5–100 µm

Model sensitivity to quartz optical properties is investigated by increasing and decreasing quartz transmissivity in the 0–2.5 µm wavelength solar band. The baseline transmissivity of quartz in the solar band given in Table 1 is 0.90. For the sensitivity investigation, model results were obtained using values of $\tau_{0\text{–}2.5\mu m}$=0.85 and 0.95. In ANSYS® Fluent®, transmissivity in a volume is implemented via an absorption coefficient [5]. Transmissivities of 0.85, 0.90, and 0.95 are equivalent to absorption coefficients for the considered quartz of 65, 42, and 20 m^{-1}, respectively. Transmissivity implemented via an absorption coefficient is a volumetric phenomenon and does not change surface reflectivity which, as mentioned, is evaluated using Snell's law and the Fresnel equations [5].

Thermal losses from results using the considered values of transmissivity are shown in Figure 8. The case in which $\tau_{0\text{–}2.5\mu m}$=0.90 is the full coverage case. Losses due to radiation remain the largest losses and decrease with increasing transmissivity. Because transmissivity via an absorption coefficient is implemented volumetrically and not at surfaces, contributions to radiative losses from reflection at the quartz surface are the same for all values of transmissivity considered. Changes in total radiative losses with changing transmissivity must therefore be due to other phenomena: either changes in magnitude of thermal emissions of the quartz volume or changes in the magnitude or transmission of thermal emissions from the receiver interior.

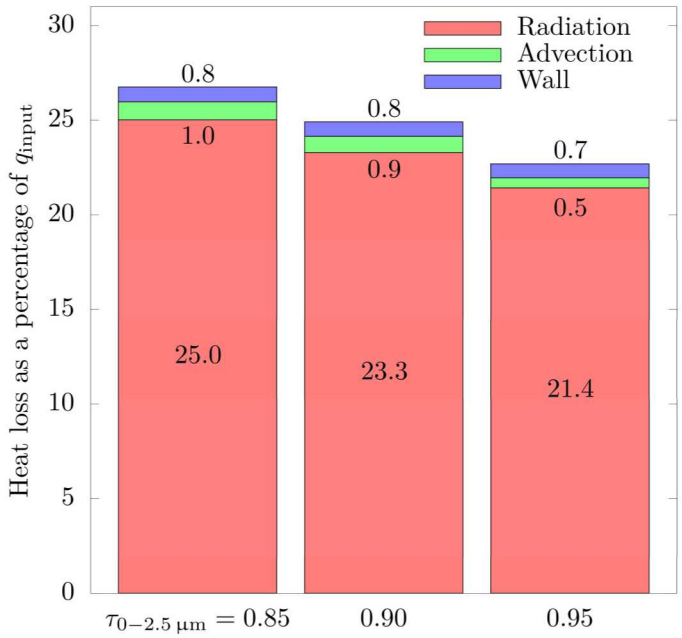

FIGURE 8: HEAT LOSS BY MECHANISM AS A PERCENTAGE OF INPUT RADIATIVE POWER ENTERING THE HOOD APERTURE FOR CASES WITH VARYING QUARTZ TRANSMISSIVITY; LOSSES ARE STACKED FROM THE BOTTOM IN THE FOLLOWING ORDER: RADIATION, ADVECTION, AND WALL

Quartz half-shell maximum and average temperatures are given in Table 6 for results using $\tau_{0\text{–}2.5\mu m}$=0.85, 0.90, and 0.95. Maximum and average temperatures decrease with increasing transmissivity. This is expected behavior, indicative of reduced absorption of radiation in the solar band by the quartz. Decreases in quartz half-shell temperature lead to observed decreases in radiative and advective losses shown in Figure 8.

Percentage of radiative losses by wavelength band are shown in Figure 9 for cases with varying quartz transmissivity. Radiative losses shift to shorter wavelengths with increasing quartz transmissivity, because a larger percentage of the radiative losses are due to the reflection of radiation in the solar band, rather than due to thermal emissions from the quartz.

Thermal efficiencies for full-aperture-coverage cases with transmissivity of 0.85, 0.90, and 0.95 are 73, 75, and 77%, respectively, shown with blue triangle points in Figure 5. The reduction of thermal losses with increasing transmissivity results in the increase in thermal efficiency with increasing transmissivity. However, the thermal efficiency of the best performing full coverage case ($\tau_{0\text{–}2.5\mu m}$=0.90, η=77%) is still less than both the thermal efficiencies of the no and half coverage cases (83 and 78%, respectively). The improvement of efficiency with increased quartz transmissivity motivates further investigation of actual optical properties of fused quartz half-shells appropriate for this application as well as the impact of even higher transmissivity values on cases with coverage.

TABLE 6: MAXIMUM AND AVERAGE QUARTZ TEMPERATURE AND THERMAL EFFICIENCY FOR CASES WITH VARYING TRANSMISSIVITY

$\tau_{0-2.5\mu m}$	0.85	0.9	0.95
T_{max}	1250°C	1170°C	1000°C
T_{avg}	1040°C	960°C	830°C

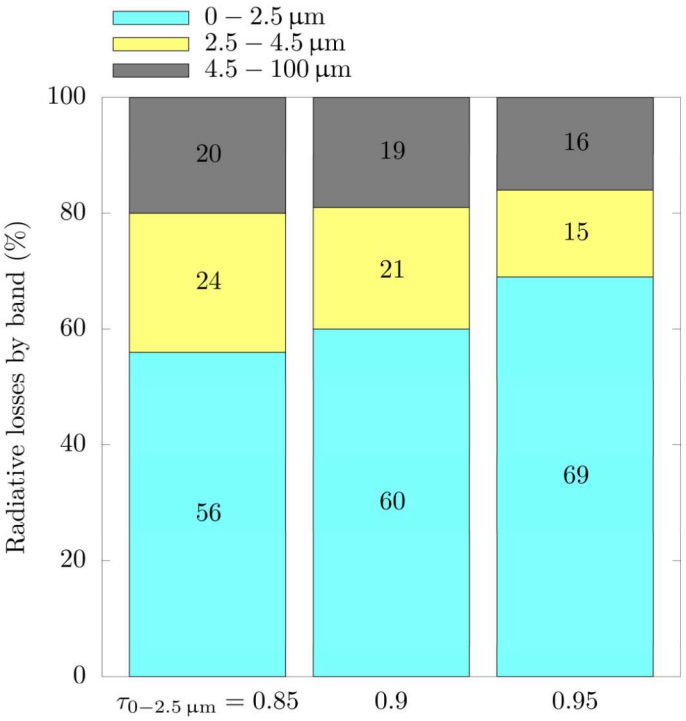

FIGURE 9: PERCENTAGE OF RADIATIVE LOSSES EVALUATED AT THE HOOD APERTURE BY WAVELENGTH BAND FOR CASES WITH VARYING QUARTZ TRANSMISSIVITY; LOSSES ARE STACKED FROM THE BOTTOM IN THE FOLLOWING ORDER: 0–2.5, 2.5–4.5, AND 4.5–100 μm

3.5 Model sensitivity to radiation spillage and receiver wall soiling

Difference in magnitude of advective losses compared to previous studies could be due to the inclusion or over prediction of radiation spillage. When spillage is included, north facing receiver temperatures are elevated and have the potential to heat air near the receiver before it enters the receiver, thereby reducing advective losses. However, elevated north facing receiver temperatures also have the potential to drive natural convection in front of the receiver, thereby increasing advective losses. The potential influence of north facing receiver wall temperatures motivates the investigation of model sensitivity to radiation spillage.

Losses due to radiation leaving the aperture are much larger than losses due to advection or through the receiver walls, contrary to previous study results of the full receiver without a hood [11]. This discrepancy between previous study results and results presented here motivates the investigation of model sensitivity to receiver wall soiling. In practice, wall soiling decreases the reflectivity of the receiver cavity. Soiling then increase wall absorption, and in this model, has the potential to decrease solar radiation reflected out of the aperture contributing to high radiative losses.

To investigate the sensitivity of model results to radiation spillage and receiver wall soiling, the following cases are considered: (1) the no coverage case with north facing receiver walls modeled as perfectly reflecting with a constant temperature of 300 K, (2) the full coverage case with an absorptivity in the solar band $\alpha_{0-2.5\ \mu m}$=0.5 for Fiberfrax® Duraboard® HD, and (3) the full coverage case with an absorptivity in the solar band $\alpha_{0-2.5\ \mu m}$=0.9 for Fiberfrax® Duraboard® HD. Cases (2) and (3) increase absorptivity from $\alpha_{0-2.5\ \mu m}$=0.1 as given in Table 2.

In case (1), changes to north wall reflectivity and temperature result in wall and advective loss percentages decreasing by less than 0.5%, radiative loss percentage increasing by less than 0.5%, and no substantial change to thermal efficiency. Changes to wall absorptivity in cases (2) and (3) results in an increase in wall loss percentage of approximately maximally 1%; a decrease in radiative loss percentage of approximately maximally 1%, and no substantial change to thermal efficiency. Based on the results of the considered cases, the model is not sensitive to radiation spillage or receiver wall soiling. Discrepancy between the dominant heat loss mechanism in the previous study of the full receiver without a hood and the work presented here have the potential to be due to the inclusion of the hood over the receiver aperture and the omission of three-dimensional cavity effects in this work.

CONCLUSIONS AND FUTURE WORK

Effects of quartz half-shell aperture covers on the fluid dynamics and thermal efficiency of the considered FPR subdomain are driven by the temperature of the quartz half-shells. In the considered system, quartz half-shell aperture covers result in decreased radiative power entering the receiver and increased radiative losses. Thus, both the thermal efficiency and net power transferred to the particles decrease with aperture coverage.

If the temperature of the quartz can be reduced by active cooling or material selection, advective and radiative losses have the potential to be reduced. Preliminary calculations show that reducing the quartz temperature reduces advective and radiative losses, and thus warrants further investigation.

Commercially available fused quartz products have transmissivities in parts of the solar band of over 98% [12], and the investigation of model sensitivity to transmissivity in Section 2.5 shows increases in quartz transmissivity will decrease thermal losses. Future work with this model will include repeating the investigation of model sensitivity to transmissivity of Section 3.4 with the half coverage case and with values of transmissivity up to 99%.

We hypothesize the existence of inflection temperatures of the quartz half-shells at which radiative losses for the considered system for the half and full coverage case are equal to those for the no coverage case. Future work will include identification of the inflection quartz half-shell temperature for a given aperture

coverage and quartz transmissivity in the solar band. This inflection temperature will guide aperture cover configurations, active cooling technique and design considerations, and material selection in future modeling and experimental work.

As discussed in Section 1.4, the radiation modeling method will be refined using ray tracing results to improve the accuracy and interrogate the accuracy of the discrete ordinate radiation model for the considered system. Evaluation of three-dimensional cavity effects will also be considered to more accurately predict radiative losses. Radiative losses in full FPR geometries are expected to be less than those predicted in this work because side wall absorption is not included in this subdomain analysis.

Future experimental work is recommended to confirm numerically predicted temperatures and loss effects. This could be accomplished with a cavity shaped calorimeter tested in a solar furnace with and without a quartz cover.

ACKNOWLEDGEMENTS

This work was funded by the DOE Solar Energy Technologies Office and Gen 3 CSP program. Sandia National Laboratories is a multimission laboratory managed and operated by National Technology and Engineering Solutions of Sandia, LLC., a wholly owned subsidiary of Honeywell International, Inc., for the U.S. Department of Energy's National Nuclear Security Administration under contract DE-NA0003525.

REFERENCES

[1] Hruby, J. M. and Steele, B. R. *Chemical Engineering Progress*, 1986

[2] Ho, C. K. *Applied Thermal Engineering*, 2016

[3] Siegel, R. and Howell, J. R., 1981 *Thermal Radiation Heat Transfer, Second edition*

[4] Ho, C. K., Christian, J. M., Yellowhair, J., Armijo, K., and Jeter, S. *Proceedings of the 2016 ASME Power & Energy Conference*, Charlotte, NC, June 26–30, 2016

[5] ANSYS® Fluent®, Release 19.2, *Theory Guide*

[6] Christian, J. and Ho, C. *Energy Procedia*, 2013

[7] Mills, B. and Ho. C. K. *Proceedings of the ASME 2017 Power & Energy Conference*, Charlotte, NC, June 26–30, 2017

[8] Mills, B. and Ho, C. K. *AIP Conference Proceedings*, 2018

[9] Siegel, N. P., Ho, C. K., Khalsa, S. S., and Kolb, G. J. *Journal of Solar Energy Engineering—Transactions of the ASME*, 2010

[10] Ho, C. K., Khalsa, S. S., and Siegel, N. P. *Proceedings of Energy Sustainability 2009*, San Francisco, CA, July 19–23, 2009

[11] Mills, B. and Ho, C. K., *24th SolarPACES International Conference*, Casablanca, Morocco, Oct 2–5, 2018

[12] Mark Optics Incorporated, www.markoptics.com

[13] Unifrax, www.unifrax.com

[14] Touloukian, Y. S. and DeWitt, D. P., 1972 *Thermal Radiative Properties: Nonmetallic Solids*

[15] Siegel, N., Kolb, G., Kim, K., Rangaswamy, V., and Moujaes, S. *Proceedings of the 2007 ASME Energy Sustainability Conference*, Long Beach, CA, July 27–30, 2007

[16] Yellowhair, J., and Ho, C. K., ES2019-3927, *Proceedings of the 2019 ASME Energy Sustainability Conference*, Belleview, WA, June 15–19, 2018